AIAA JOURNAL
Vol. 36, No. 6, June 1998

# Reduced-Order Modeling of Unsteady Viscous Flow in a Compressor Cascade

Razvan Florea,* Kenneth C. Hall,† and Paul G. A. Cizmas‡
*Duke University, Durham, North Carolina 27708-0300*

**A simultaneously coupled viscous–inviscid interaction (VII) analysis is used to model the unsteady viscous separated flow through a subsonic compressor. The inner viscous flow around the airfoil and in the wake is modeled using a finite difference discretization of the boundary-layer equations and a one-equation turbulence transport model. The outer inviscid flow is modeled using a variational finite element discretization of the compressible full potential equation. The viscous and inviscid regions are simultaneously coupled using a injection type boundary condition along the airfoil and wake. The resulting nonlinear unsteady equations are linearized about the nonlinear steady flow to obtain a set of linear equations that describe the unsteady small-disturbance behavior of the viscous flow through the cascade. The discretized small-disturbance VII equations are used to form a generalized, quadratic, non-Hermitian eigenvalue problem that describes the eigenmodes (natural modes) and eigenvalues (natural frequencies) of fluid motion about the cascade. Using a Lanczos algorithm, the eigeninformation is computed efficiently for various steady flow inflow angles and unsteady interblade phase angles. The eigenvalues and eigenmodes are then used in conjunction with a classical mode summation technique to construct computationally efficient reduced-order models of the unsteady flow through the cascade. Using just a few eigenmodes, less than 0.01% of the total number, the unsteady aerodynamic loads acting on vibrating airfoils (the aeroelastic stability problem) can be efficiently and accurately computed over a relatively wide range of reduced frequencies provided that one or more static corrections are performed. Finally, the eigenvalues and eigenvectors provide physical insight into the unsteady aerodynamic behavior of the cascade. For example, we show the ability of the present eigenanalysis to predict purely fluid mechanic instabilities such as rotating stall.**

## I. Introduction

STALL flutter and rotating stall place fundamental limitations on aircraft engine performance and remain persistent problems in the development of axial compressor and fan stages. Rotating stall is a purely fluid mechanic instability, whereas stall flutter is an aeroelastic instability involving both blade vibration and fluid motion. Both stall flutter and rotating stall tend to occur when the blades of a compressor or fan are operating at high-incidence angles and/or part speed, and it is believed that unsteady viscous flow separation plays a key roll in both of these phenomena.[1–3]

Most unsteady aerodynamic models used in industry do not adequately model the essential unsteady flow separation or, on the other hand, are computationally expensive. For example, time-marching Navier–Stokes solvers are perhaps the most sophisticated models available to predict unsteady flow separation. They have the added advantage that they are relatively straightforward to implement, and they can model both linear and nonlinear unsteady flows. However, time-marching Navier–Stokes codes are computationally too expensive for use in routine design studies. Furthermore, they provide little physical insight into the nature of unsteady cascade flows other than through expensive and time-consuming parametric studies. Also, Navier–Stokes models have many thousands of degrees of freedom making them difficult to use in the design of active control systems for the prevention of rotating stall and flutter, a topic of increasing interest. What is needed are so-called reduced-order models of the unsteady flow in cascades, models that contain a small number of degrees of freedom but nevertheless can accurately predict unsteady flows.

Presented as Paper 96-2572 at the AIAA/ASME/SAE/ASEE 32nd Joint Propulsion Conference, Lake Buena Vista, FL, July 1–3, 1996; received July 25, 1996; revision received Jan. 20, 1998; accepted for publication Jan. 25, 1998. 

*Assistant Research Professor, Department of Mechanical Engineering and Materials Science. Member AIAA.

†Associate Professor, Department of Mechanical Engineering and Materials Science. Associate Fellow AIAA.

‡Graduate Research Assistant, Department of Mechanical Engineering and Materials Science; currently Senior Engineer/Scientist, Westinghouse Science and Technology Center, Pittsburgh, PA 15235-5098. Member AIAA.

Over the years, researchers have used a variety of reduced-order models to analyze unsteady flows. Reduced-order modeling techniques can be grouped into two broad categories: simplified physical models and mathematically reduced computational fluid dynamic models. In the case of simplified physical models, gross simplifications of the fluid mechanics in a cascade are made based on some physical insight into the nature of the unsteady flow. Examples of this approach include Whitehead's[4,5] actuator-disk theories for incompressible unstalled flutter. Kaji and Okazaki[6] developed semiactuator disk theories for subsonic unstalled flutter. Adamczyk et al.[7] and more recently Gysling and Myers[8] incorporated empirical correlations of pressure rise characteristics into actuator disk theories to produce low-order models of stall flutter. Similarly, Greitzer[2] and Moore and Greitzer[3] developed semi-empirical semiactuator disk models of rotating stall and surge. Such physically based, reduced models have the advantage that the unsteady aerodynamic behavior is described by a small set of equations and, thus, are computationally quite efficient. Furthermore, the simplicity of these models provides physical insight in the fundamental physical mechanisms at work (or perhaps it is the physical insight of the aerodynamicist that provides the simplification). However, the assumptions on which these models are built restrict their applicability to low frequencies and low interblade phase angles. Thus, although they are well suited for the rotating stall problem, they are of limited accuracy for the stall flutter problem that typically occurs at moderate reduced frequencies (of order unity) and moderate interblade phase angles, i.e., not necessarily close to zero. Furthermore, because the physically based models are ad hoc, it is difficult to estimate a priori the errors introduced by the modeling assumptions or to predict certain flow features in detail, e.g., the motion of the separation point on the airfoil.

A number of investigators have developed mathematically derived reduced-order models. One approach is essentially to curve fit the unsteady aerodynamic transfer function.[9–13] The approximate time-domain representation is usually taken to be a sum of exponentials so that the resulting Laplace transform is a rational polynomial. The parameters in the approximation, such as the time constant of the exponentials or the constant multiplying each exponential, are found by minimizing the error between the approximation and the exact solution at a finite number of frequencies. This approach has a

number of difficulties. For example, the process must be repeated for each type of blade motion (pitching, plunging, etc.). Also, although mathematically useful, this sort of curve fitting provides little insight into the physics of the unsteady flowfield because no modal information is obtained.

More recently, a number of reduced-order models have been developed based on classical eigenmode summation techniques. Using this approach, the unsteady flow about a cascade of airfoils, or about an isolated wing or airfoil, is assumed to be composed of eigenmodes (natural modes of fluid motion), each mode corresponding to an eigenvalue (natural frequency of fluid motion). The eigenmodes and eigenvalues are found by solving a large sparse eigenvalue problem based on the discretized flow equations. Mahajan et al.[14] computed the eigenvalues of unsteady flow over isolated airfoils. The unsteady flow was modeled with a nonlinear Navier–Stokes solver. Hall[15] computed the eigenvalues and eigenvectors of an unsteady incompressible vortex lattice model of flows about two-dimensional cascades and isolated airfoils and then used this information to construct reduced-order models. Hall et al.[16] and Florea and Hall[17] constructed eigenmode-based reduced-order models of time-linearized frequency-domain unsteady compressible flow about two-dimensional cascades and an isolated airfoil. Around the same time, Romanowski and Dowell[18,19] developed reduced-order models based on the eigenmodes of a linearized time-domain Euler solver.

In this paper, we develop a computationally efficient reduced-order model of unsteady two-dimensional viscous flows in cascades based on the classical mode summation method. Toward that end, we first develop a simultaneously coupled viscous–inviscid interaction (VII) model of unsteady flow in cascades. The model is similar to one originally developed by Cizmas and Hall[20,21] but differs in that the present model uses the one-equation Spalart–Allmaras[22] turbulence model rather that the algebraic Cebeci–Smith model[23] and the effect of wake curvature is taken into account. We use the VII model and the accompanying reduced-order modeling technique to investigate both fluid–structure instabilities (flutter) and purely fluid dynamic instabilities, e.g., rotating stall. We show that the unsteady aerodynamic response associated with stall flutter can be accurately represented with just a handful of fluid eigenmodes, provided that one or more so-called static corrections are used to account for the neglected eigenmodes. Moreover, the eigenfrequencies and eigenmodes themselves provide physical insight into the behavior of the unsteady flow. For example, we are able to predict what appears to be rotating stall using the present method.

## II. Theory

To predict the details of stall flutter and/or rotating stall in turbomachinery cascades, it is essential to model unsteady flow separation. Fortunately, for many cases of practical interest, viscous effects are confined to thin regions near the airfoil surface and wake. Under these circumstances, the flow can be divided into an inviscid outer region and a viscous inner region. The governing equations of motion are discretized on separate computational grids in each of these two regions (see, e.g., Fig. 1). The two regions are then coupled together by matching boundary conditions at the inner boundary of the outer flow and the outer boundary of the inner flow. Commonly used coupling procedures may be classified under the following categories: direct, inverse,[24] semi-inverse,[25–29] quasisimultaneous,[30] and simultaneous.[20,21,31–34] With the exception of the direct coupling, all these coupling procedures can be used for solving flows with separation. The method described in the following is based on the simultaneous coupling described in Refs. 20, 21, and 34.

### A. Inviscid Outer Flow

In this paper, we model low-speed flow in a compressor. The outer flow is assumed to be inviscid, irrotational, two-dimensional, and non-heat-conducting and to have constant specific heats. Because the flow is irrotational, the velocity may be represented as the gradient of a scalar velocity potential $\hat{\phi}$. The inviscid flow is governed by the well-known unsteady full potential equation, i.e.,

$$\nabla^2\hat{\phi} = \frac{1}{\hat{c}^2}\left[\frac{\partial^2\hat{\phi}}{\partial t^2} + 2\nabla\hat{\phi}\cdot\nabla\frac{\partial\hat{\phi}}{\partial t} + \frac{1}{2}\nabla\hat{\phi}\cdot\nabla(\nabla\hat{\phi})^2\right] \tag{1}$$

where $\hat{c}$ is the local speed of sound equal to $\sqrt{(\gamma\hat{p}/\hat{\rho})}$ and $\hat{\rho}$ and $\hat{p}$ are the static density and pressure, respectively. We note that the equation is hyperbolic in time and nonlinear in the unknown velocity potential $\hat{\phi}$.

### B. Viscous Inner Flow

We consider only low-speed flow. For simplicity and computational efficiency, we assume that the inner viscous flow is incompressible. Thus, the conservation of mass is given by

$$\frac{\partial\hat{u}}{\partial s} + \frac{\partial\hat{v}}{\partial n} = 0 \tag{2}$$

where $\hat{u}$ and $\hat{v}$ are the components of velocity in the directions parallel (streamwise) and normal to the airfoil surface and wake centerline and $s$ and $n$ are the distances parallel to and normal to these surfaces, respectively.

Making the usual Prandtl thin boundary-layer assumptions, the conservation of momentum in the streamwise direction is expressed as

$$\rho_0\left(\frac{\partial\hat{u}}{\partial t} + \hat{u}\frac{\partial\hat{u}}{\partial s} + \hat{v}\frac{\partial\hat{u}}{\partial n}\right) = \frac{\partial}{\partial n}\left(\mu\frac{\partial\hat{u}}{\partial n} - \rho_0\overline{\hat{u}'\hat{v}'}\right) - \frac{\partial\hat{p}_e}{\partial s} - \rho_0\frac{\partial^2 q_a}{\partial t^2} \tag{3}$$

where $\rho_0$ is the (constant) static density in the boundary layer, $\mu$ is the absolute viscosity, and the subscript $e$ denotes outer flow quantities at the inner boundary. Note that $s$ and $n$ are defined with respect to coordinates attached to the airfoil surface. Thus, there is a D'Alembert body force on the right-hand side of Eq. (3) arising from the motion of the airfoil ($q_a$ is the displacement of the airfoil in the

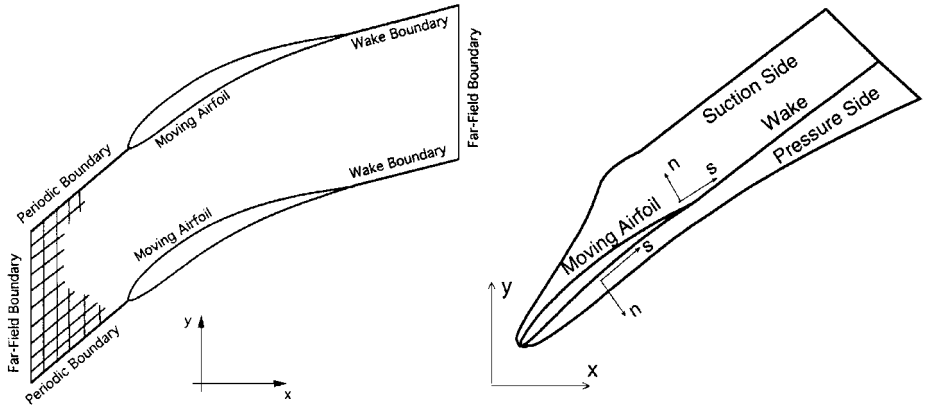


**a) Inviscid outer flow domain** **b) Inner viscous flow domain around airfoil and wake**

**Fig. 1 Computational domains used to compute flow through cascade.**

streamwise direction). The pressure gradient term on the right-hand side of Eq. (3) is given by

$$\frac{\partial \hat{p}_e}{\partial s} = -\hat{\rho}_e\left(\frac{\partial \hat{u}_e}{\partial t} + \hat{u}_e\frac{\partial \hat{u}_e}{\partial s} + \frac{\partial^2 q_a}{\partial t^2}\right) \tag{4}$$

Finally, $\rho_0\overline{\hat{u}'\hat{v}'}$ is the Reynolds stress due to turbulent velocity fluctuations $u'$ and $v'$.

It will be convenient here to introduce a coordinate rescaling in the normal direction. We let

$$s = s, \qquad \zeta = n/l^* \tag{5}$$

where $l^*$ is a characteristic boundary-layer thickness, which may vary with $s$, and is taken here to be approximately equal to $\hat{\delta}^*$, the boundary-layer displacement thickness. This coordinate transformation permits us to use a relatively small number of computational cells in the normal direction, for example, on the order of 39 or less.

To reduce the number of unknowns in the momentum equation, we introduce the stream function $\hat{\Psi}$. Thus,

$$\hat{u} = \frac{\partial \hat{\Psi}}{\partial n}, \qquad \hat{v} = -\frac{\partial \hat{\Psi}}{\partial s} \tag{6}$$

The velocities obtained is this way automatically satisfy the continuity equation (2). Next, we define the nondimensional stream function $\hat{f}$ such that

$$\hat{f}(s, \zeta, t) = \hat{\Psi}\big/u_0 l^* \tag{7}$$

where $u_0$ is a characteristic velocity taken here to be the magnitude of the upstream far-field steady velocity $V$. Combining Eqs. (3–7) gives

$$\frac{1}{L^{*2}}(\hat{b}\hat{f}'')' + \frac{1}{L^*}\frac{\partial L^*}{\partial s}\hat{f}\hat{f}'' + \frac{\hat{\rho}_e}{\rho_0}\frac{1}{u_0^2}\left(\frac{\partial \hat{u}_e}{\partial t} + \hat{u}_e\frac{\partial \hat{u}_e}{\partial s}\right) = \frac{1}{u_0}\frac{\partial \hat{f}'}{\partial t} + \hat{f}'\frac{\partial \hat{f}'}{\partial s} - \hat{f}''\frac{\partial \hat{f}}{\partial s} \tag{8}$$

where the primes denote differentiation with respect to $\zeta$. Also, in Eq. (8) we define the following quantities:

$$L^* = l^*\sqrt{u_0/\nu}$$

and

$$\hat{b} = 1 + \hat{\epsilon} = 1 + (\hat{\nu}_t/\nu)$$

where $\nu$ and $\hat{\nu}_t$ are the molecular and turbulent kinematic viscosities, respectively.

In this investigation, a slightly modified Spalart–Allmaras[22] turbulence model (their version Ia) is used to compute the eddy viscosity term $\hat{b}$ (for a summary of the model, see the Appendix of Ref. 22). The original Spalart–Allmaras model is a one-equation transport equation derived using a combination of empiricism and physical modeling. Again, we make the usual Prandtl boundary-layer assumptions to convert the turbulence model to a boundary-layer form. The Spalart–Allmaras model incorporates a trip function, which requires the user to specify a boundary-layer trip point on the airfoil; we place trip points just aft of the stagnation point on both the pressure and suction surfaces.

We have found that, in some cases, the turbulent viscosity $\nu_t$ becomes too small near the outer edge of the boundary layer, causing numerical difficulties. Therefore, we set the turbulence in this region to $\max(\nu_{t\mathrm{SA}}, \alpha\nu\hat{\delta}^*\hat{u}_e)$. The second of these two terms is similar in form to the Cebeci–Smith[23] turbulence model, but the coefficient $\alpha$ used in the present study is considerably smaller than that value of 0.0168 used in the Cebeci–Smith model; we choose $\alpha$ large enough to suppress spurious oscillations at the outer edge of the boundary layer but small enough not to affect significantly the solution.

### C. Boundary Conditions

Boundary conditions are required to complete the problem specification. On airfoil surfaces, the no-slip condition applies. This requires that at $\zeta = 0$

$$\hat{f} = \hat{f}' = 0 \tag{9}$$

Similarly, the turbulent viscosity is prescribed to be zero on the airfoil surfaces. Also, we require that the velocities and turbulent viscosity be continuous across the centerline of the wake, i.e., at $\zeta = 0$, where the upper and lower wake grids are connected.

At the edge of the boundary layer, the velocity at the outer boundary of the inner region must match the potential edge velocity at the inner boundary of the outer region, so that

$$u_0\hat{f}'\Big|_{\zeta\to\infty} = \hat{u}_e = \frac{\partial \hat{\phi}}{\partial s}\Big|_{n=0} - \frac{\partial q_a}{\partial t} \tag{10}$$

In other words, the potential velocity at the airfoil surface is equal to the boundary-layer velocity far from the airfoil surface, taken here to be approximatively six to nine times the characteristic thickness $l^*$. The flow in the stagnation region is assumed to be laminar. Hence, in the steady case, the flow is similar and the quantity $\delta^*[(\partial u_e/\partial s)/\nu]^{1/2}$ is a constant equal to approximatively 0.648 (Ref. 23). For the unsteady flow, the flow in the stagnation region at the stagnation point is assumed to be quasisteady. Whereas the position of the trip point may affect both the steady and unsteady solutions, in the present study this effect is not investigated. The level of freestream turbulence in the flow is simply assumed to be large enough so that the flow trips immediately after the stagnation region. At points aft of the trip point, the turbulent viscosity is set to a small but nonzero value at the edge of the boundary layer.

The influence of the inner viscous flow on the outer inviscid flow is modeled with an injection boundary condition on the surface of the airfoil, i.e.,

$$Q = \hat{\rho}_e\frac{\partial \hat{\phi}}{\partial n}\Big|_{n=0} \frac{\partial}{\partial s}\left(\hat{\rho}_e\hat{u}_e\hat{\delta}^*\right) + \hat{\rho}_e\frac{\partial \hat{r}}{\partial t} \tag{11}$$

where $\hat{r}$ is the displacement of the airfoil normal to the airfoil surface. A similar condition is applied on either side of the wake. On the suction surface side of the wake, we have

$$Q = \hat{\rho}_e\frac{\partial \hat{\phi}}{\partial n}\Big|_{n=0} = \frac{\partial}{\partial s}\left(\hat{\rho}_e\hat{u}_e\hat{\delta}^*\right) + \hat{\rho}_e\left(\frac{\partial \hat{r}_w}{\partial t} + \frac{\partial \hat{\phi}}{\partial s}\frac{\partial \hat{r}_w}{\partial s}\right) \tag{12}$$

where $\hat{r_w}$ is the displacement of the wake centerline normal to an original reference position. Similarly, on the pressure surface side,

$$Q = \hat{\rho}_e\frac{\partial \hat{\phi}}{\partial n}\Big|_{n=0} = \frac{\partial}{\partial s}\left(\hat{\rho}_e\hat{u}_e\hat{\delta}^*\right) - \hat{\rho}_e\left(\frac{\partial \hat{r}_w}{\partial t} + \frac{\partial \hat{\phi}}{\partial s}\frac{\partial \hat{r}_w}{\partial s}\right) \tag{13}$$

To provide closure for the wake position, and to provide the viscous equivalent of a Kutta condition, we require that $\hat{r}_w$ be equal to the displacement of the trailing edge normal to the reference wake line. We also impose a pressure jump across the wake that takes into account the curvature of the wake centerline.

Upstream and downstream of the cascade, flow periodicity is enforced. In the case of unsteady flows, the unsteady flow perturbations satisfy a complex periodicity condition that requires that flow perturbations be equal in magnitude from one blade passage to the next, but shifted in phase by the interblade phase angle $\sigma$. This complex periodicity condition allows the computational domain to be reduced to a single blade passage.

Finally, far-field boundary conditions must be applied at the upstream and downstream boundaries of the inviscid outer flow computational domain. For steady flows, the total pressure, total density, and circumferential velocity are prescribed upstream while the mass flux is prescribed downstream. For unsteady flows, numerically exact nonreflecting boundary conditions are applied in the conventional analysis.[35]

## III. Steady and Linearized Unsteady Flow Solvers

In this section, we briefly describe the conventional steady and unsteady flow solvers and give some computational results. We defer until Sec. IV the main topic of this paper, that is, the use of reduced-order modeling techniques.

### A. Linearization

The governing equations of unsteady fluid motion are nonlinear, making them difficult to solve except by direct time-marching techniques. However, we are interested in the onset of instabilities and not the large-amplitude behavior. Thus, it is sufficient to solve for the unsteady flow while disturbances are still small. In this section, we describe the linearization of the unsteady flow equations.

#### 1. *Outer Flow Linearization*

To begin, we consider the potential outer flow. To improve the accuracy of the potential solver, a harmonically deforming computational grid that conforms to the motion of the airfoil will be used.[36] Thus, we make the coordinate transformation

$$x(\xi, \eta, \tau) = \xi + g(\xi, \eta)\exp(j\omega\tau) \tag{14}$$

$$y(\xi, \eta, \tau) = \eta + h(\xi, \eta)\exp(j\omega\tau) \tag{15}$$

$$t(\xi, \eta, \tau) = \tau \tag{16}$$

where $\xi$ and $\eta$ are coordinates attached to the deforming computational grid and $g$ and $h$ are the complex amplitudes of the harmonic displacement of the grid in the $x$ and $y$ directions, respectively. Similarly, the unsteady potential flow is decomposed into a nonlinear mean flow potential $\Phi$ and a linear unsteady perturbation potential $\phi$, so that

$$\hat{\phi}(\xi, \eta, \tau) = \Phi(\xi, \eta) + \phi(\xi, \eta)\exp(j\omega\tau) \tag{17}$$

Substitution of these perturbation series into the full potential equation (1) and collection of terms of zeroth and first order in the perturbation quantities produces the desired steady and unsteady potential equations. The steady flow is governed by

$$\nabla'^2\Phi = (1/C^2)\left[\tfrac{1}{2}\nabla'\Phi \cdot \nabla'(\nabla'\Phi)^2\right] \tag{18}$$

where $\nabla'$ is the gradient operator $(\partial/\partial\xi, \partial/\partial\eta)^T$. Similarly, the linear equation for the complex amplitude of the disturbance potential

$$\nabla' \cdot R\nabla'\phi - \nabla' \cdot [(R/C^2)(\nabla'\Phi \cdot \nabla'\phi + j\omega\phi)\nabla'\Phi] - (R/C^2)(j\omega\nabla'\Phi \cdot \nabla'\phi - \omega^2\phi) = d(\xi, \eta) \tag{19}$$

where $R$ and $C$ are the steady flow density and speed of sound, respectively, and $d$ is an inhomogeneous term arising from the blade motion and resulting grid deformation.

#### 2. *Inner Flow Linearization*

Similarly, the boundary-layer equations and turbulence model equations are linearized by letting

$$\hat{f}(s, n, \tau) = F(s, n) + f(\xi, \eta)\exp(j\omega\tau) \tag{20}$$

$$\hat{b}(s, n, \tau) = B(s, n) + b(s)\exp(j\omega\tau) \tag{21}$$

$$\hat{u}_e(s, \tau) = U_e(s, n) + u_e(s)\exp(j\omega\tau) \tag{22}$$

$$\hat{\delta}^*(s, \tau) = \Delta^*(s) + \delta^*(s)\exp(j\omega\tau) \tag{23}$$

Substitution of these assumptions into the boundary-layer equation (8), and again collecting terms of equal order, gives the steady and linearized unsteady boundary-layer equations. The steady boundary-layer equation is given by

$$\frac{1}{L^{*2}}(BF'')' + \frac{1}{L^*}\frac{\partial L^*}{\partial s}FF'' + \frac{R_e}{\rho_0}\frac{1}{u_0^2}U_e\frac{\partial U_e}{\partial s} = \left(F'\frac{\partial F'}{\partial s} - F''\frac{\partial F}{\partial s}\right) \tag{24}$$

The linearized unsteady boundary-layer equation is

$$\frac{1}{L^{*2}}[(Bf'')' + (bF'')'] + \frac{1}{L^*}\frac{\partial L^*}{\partial s}(Ff'' + fF'') + \frac{R_e}{\rho_0}\frac{1}{u_0^2} \times \left(j\omega u_e + U_e\frac{\partial u_e}{\partial s} + u_e\frac{\partial U_e}{\partial s}\right) + \frac{\rho_e}{\rho_0}\frac{1}{u_0^2}U_e\frac{\partial U_e}{\partial s} = \frac{1}{u_0^2}\frac{\partial^2 q_a}{\partial t^2} + \left[\frac{j\omega}{U_e}f' + \left(F'\frac{\partial f'}{\partial s} + f'\frac{\partial F'}{\partial s}\right) - \left(f''\frac{\partial F}{\partial s} + F''\frac{\partial f}{\partial s}\right)\right] \tag{25}$$

A similar linearization of the modified Spalart–Allmaras turbulence model has been performed, but the results are omitted here because of their complexity.[34] Finally, the boundary conditions described in Sec. II.C are linearized in a completely analogous fashion.

### B. Numerical Solution Technique

The numerical solution procedure is a two-step process. First, the steady nonlinear flow is computed. An outer inviscid H-grid of quadrilateral elements (Fig. 1a) is generated using a combination of algebraic and elliptic grid generation techniques. The nonlinear steady full potential equation (1) is discretized using a variational finite element method developed by Hall[36] that is based on a variational principle for compressible flow proposed by Bateman.[37] The inner viscous grid is generated algebraically, and is rectangular in the $(s, \zeta)$ coordinate system (Fig. 1b). The Keller and Cebeci[38] box scheme is used to discretize the steady boundary-layer equation (8). A central difference scheme is used to discretize the Spalart–Allmaras turbulence transport equation.

Having discretized the inner and outer flows, the two regions are then coupled together through the matching boundary conditions, which are discretized using a combination of finite difference and finite element techniques. The result is a large set of nonlinear equations, which are solved using Newton iteration. Because the discretized flow model is strongly nonlinear, underrelaxation must be used in the initial iterations. Typically, on the order of 50–100 iterations are required to obtain converged solutions for flows with moderate to fairly large boundary-layer separations.

In the second step of the solution procedure, the linearized potential, boundary-layer, and turbulence transport equations and the boundary conditions are discretized. Again, a combination of finite element and finite difference techniques are used to discretize the equations. The result is a set of linear equations of the form

$$\boldsymbol{Au} = \boldsymbol{b} \tag{26}$$

where $\boldsymbol{u}$ is the vector containing the unknown unsteady flow perturbation quantities, primarily the nodal values of $\phi$ on the outer grid and $f$, $f'$, and $f''$ on the inner grid, plus some auxiliary variables such as $\delta^*$ defined at each streamwise station on the inner grid. The matrix $\boldsymbol{A}$ is a large sparse, complex, non-Hermitian matrix that is a function of the steady flow solution and the prescribed frequency $\omega$ and interblade phase angle $\sigma$ of blade motion. The vector $\boldsymbol{b}$ is an inhomogeneous term arising from the prescribed blade motion.

Finally, Eq. (26) is solved using lower–upper (LU) matrix decomposition with one forward and one backward substitution. This approach is reasonably efficient with each linearized solution requiring just a few minutes of CPU time on a modern workstation computer.

### C. Computational Results

Next, we present numerical solutions of the steady and linearized unsteady VII models. In particular, the flow through a modified Tenth Standard Configuration cascade is considered. The Tenth Standard Configuration is a generic compressor cascade geometry defined at the 6th International Symposium on Unsteady Aerodynamics and Aeroelasticity of Turbomachines.[39] The airfoils in the cascade have a circular arc camber line with 5% camber and a slightly modified NACA 0006 thickness distribution. The stagger angle $\theta$ of the airfoils is 45 deg, and the gap-to-chord ratio $G$ is 1.0. The inflow angle of the lower-speed Tenth Standard Configuration is $\Omega = 55$ deg, and the inflow Mach number $M$ is 0.7. However, because the present investigation is limited to low-speed flows, we take the inflow Mach number to be 0.3 and the inflow angle $\Omega$ is varied from 55 to 61.5 deg. The Reynolds number $Re_c$ based on upstream velocity $V$ and airfoil chord $c$ is $10^5$.

Three composite computational grids are used in the computations (see Fig. 1). The coarse grid is composed of a $65 \times 17$ node outer H grid (65 in the streamwise direction and 17 in the crossflow direction), plus a $51 \times 39$ node boundary-layer grid on the suction surface and upper half of the wake and a $51 \times 37$ node boundary-layer grid on the the pressure surface and lower half of the wake. The medium grid is composed of a $96 \times 22$ node outer H grid, plus $75 \times 39$ and $75 \times 37$ node boundary-layer grids. The fine grid

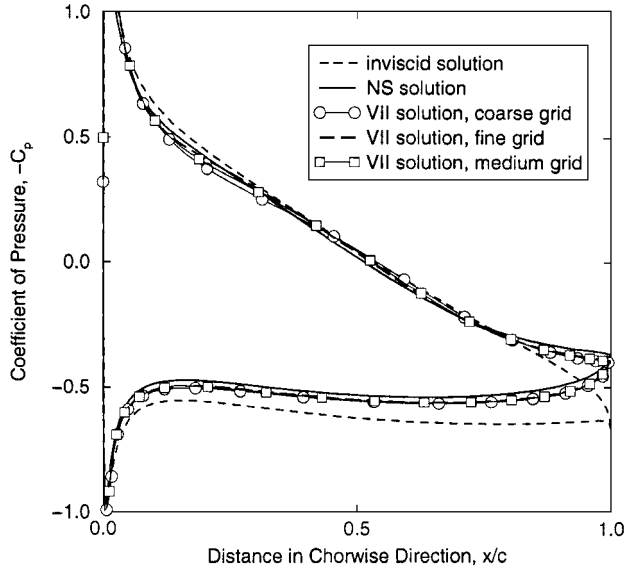


**Fig. 2 Coefficient of pressure of steady flow through modified Tenth Standard Configuration for different grids and different flow solvers, $\Omega = 60$ deg.**

is composed of a $126 \times 22$ node outer H grid plus $102 \times 39$ and $102 \times 37$ node boundary-layer grids.

*1. Steady Flow in a Low-Speed Compressor*

We first consider the steady flow through the cascade. The surface pressure coefficient on three different grids computed with the VII flow solver is compared in Fig. 2 with results obtained with the Navier–Stokes analysis of Clark (see the Acknowledgments) for the inflow angle $\Omega = 60$ deg. Also shown is the pressure coefficient computed using the inviscid flow solver of Hall.[36] The Navier–Stokes flow solver uses the same Spalart–Allmaras turbulence model used in this investigation. The VII results demonstrate that the solution is grid converged. Note that there are small differences between the coarse and the fine grid solutions but the medium and the fine grid solutions are practically indistinguishable. Hence, in all of the subsequent calculations we use the medium grid. Figure 2 also shows good agreement between the present method and the Navier–Stokes solver over most of the airfoil surface. On the suction side of the airfoil, some small discrepancies between the two viscous solutions are seen, especially in the separation region, near the trailing edge. Hence, the pressure level on the pressure surface of the airfoil is also affected because the circulation about the airfoil is fixed by the degree of flow separation. Overall, however, the present method gives quite acceptable solutions.

Figure 3 shows the computed pressure coefficient, boundary-layer displacement thickness, and skin-friction coefficient of the surface of the airfoil and in the wake for three different inflow angles, $\Omega = 55$, 60, and 61.5 deg. Note from the skin-friction plot that the flow is separated for all of these incidence angles, and the trailing-edge separation point moves forward as the inflow angle is increased. Also, at the largest inflow angle, a small leading-edge separation bubble is seen.

*2. Unsteady Flow in a Low-Speed Compressor*

Next we consider the unsteady aerodynamic response of the cascade due to pitching motion of the airfoils with fixed amplitude $\alpha$, interblade phase angle $\sigma$, and frequency $\omega$. The pitch axis of each airfoil is a point located near the midchord, $(x/c, y/c) = (0.5, 0.05)$. The reduced frequency of pitching motion, defined by $\bar{\omega} = \omega V/c$, where $V$ is the magnitude of the upstream relative velocity, is 1.0. Shown in Fig. 4 are the real and imaginary (in-phase and out-of-phase) components of the unsteady aerodynamic pitching moment acting on the reference airfoil and measured about the pitch axis for several different inflow angles $\Omega$ at two reduced frequencies, $\bar{\omega} = \omega c/V$ for a range of interblade phase angles $\sigma$. In our notation, a tuned cascade will be aeroelastically unstable whenever the imaginary part of the moment is positive, that is, the aerodynamic

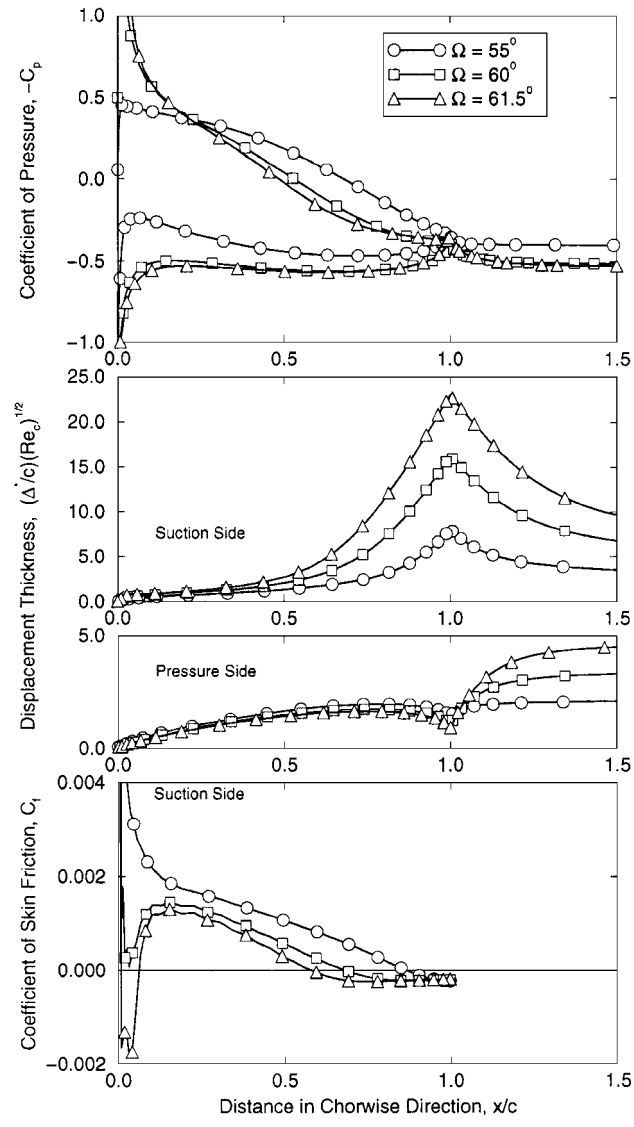


**Fig. 3 Computed surface quantities for steady flow through modified Tenth Standard Configuration; top to bottom: pressure coefficient, boundary-layer displacement thickness, and skin friction coefficient.**

damping is negative. Note that the (viscous) cascade is generally less stable at the lower reduced frequency ($\bar{\omega} = 0.5$), and there is a dramatic decrease in stability as the incidence increases. This instability may be properly called stall flutter because there is a significant loss in stability with only a small change in incidence. Furthermore, this loss in stability is coincident with the rapid increase in flow separation. Although not shown here for all different inflow angles, an inviscid analysis predicts the rotor to be aeroelastically stable over the range of parameters examined. These results are qualitatively similar to ones obtained by Clark and Hall.[40]

## IV. Reduced-Order Modeling

### A. Theory

Except for the nonreflecting boundary conditions in their original form, all of the terms in the discretized time-linearized equation (26) are quadratic in the frequency $\omega$. The terms arising from the far-field boundary conditions are approximated by a quadratic curve fit over a specified frequency range $0 \leq \omega \leq 1$ in our analysis. The resulting matrix equation is given by

$$\left[\boldsymbol{A}_0 + j\omega\boldsymbol{A}_1 + \omega^2\boldsymbol{A}_2\right]\boldsymbol{u} = \boldsymbol{b} \tag{27}$$

where the matrices $\boldsymbol{A}_0$, $\boldsymbol{A}_1$, and $\boldsymbol{A}_2$ are $m \times m$ matrices that are dependent on the mean flow solution and the prescribed interblade phase angle but independent of the excitation frequency $\omega$. The vector $\boldsymbol{b}$ arises from the prescribed blade motion. In this form, it is clear that the fluid dynamic stability of the system is governed by

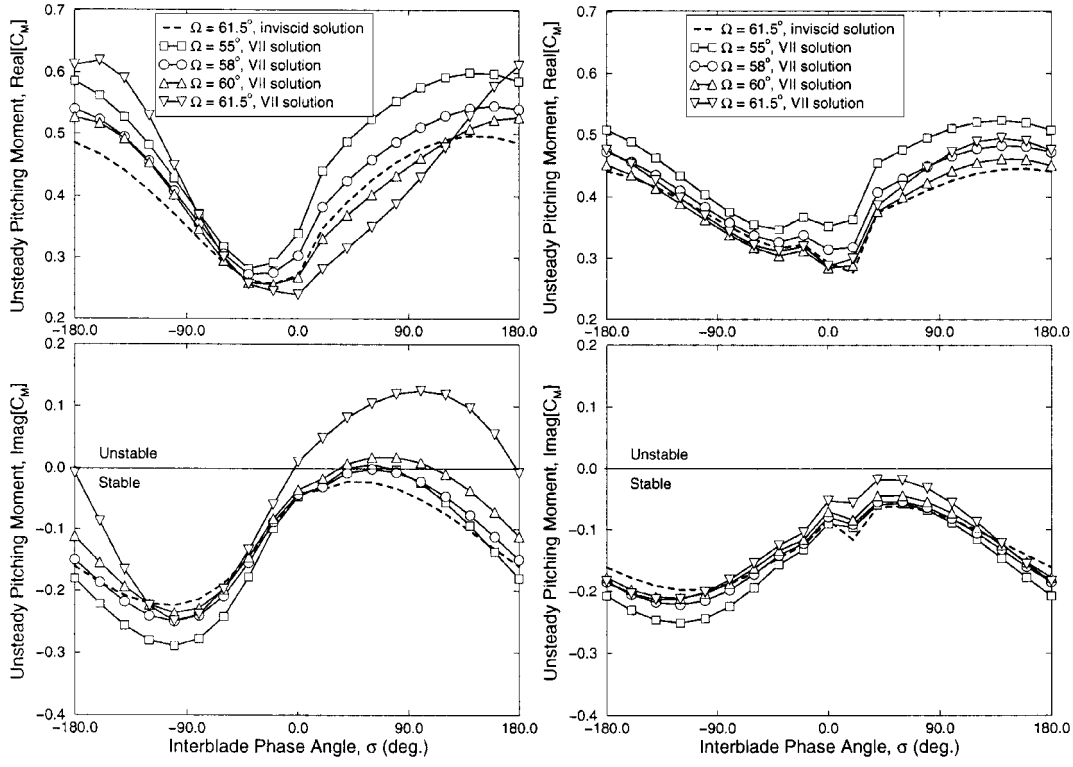


a) $\bar{\omega} = 0.5$ b) $\bar{\omega} = 1.0$

**Fig. 4 Real and imaginary parts of the aerodynamic pitching moment due to pitching of the airfoils about a point near their midchords.**

a second-order eigenvalue problem in $\omega$. The aeroelastic stability problem, on the other hand, is determined by the particular solution of Eq. (27).

For many applications, it will be convenient to construct reduced-order models of the unsteady flow. Toward that end, we compute the dominant (low-frequency) eigenvalues and corresponding eigenmodes of the the homogeneous part of Eq. (27) and use the eigeninformation to form low-degree-of-freedom models. To start, we first convert Eq. (27) from a second-order equation in $\omega$ to a first-order equation by defining the state vector

$$\boldsymbol{U} = \begin{Bmatrix} j\omega\boldsymbol{u} \\ \boldsymbol{u} \end{Bmatrix} \tag{28}$$

Thus, Eq. (28) may be rewritten as

$$\mathcal{A}\boldsymbol{U} - j\omega\mathcal{B}\boldsymbol{U} = \bar{\boldsymbol{b}} \tag{29}$$

where

$$\mathcal{A} = \begin{bmatrix} \boldsymbol{G} & \boldsymbol{0} \\ \boldsymbol{A}_1 & \boldsymbol{A}_0 \end{bmatrix}, \qquad \mathcal{B} = \begin{bmatrix} \boldsymbol{0} & \boldsymbol{G} \\ \boldsymbol{A}_2 & \boldsymbol{0} \end{bmatrix}, \qquad \bar{\boldsymbol{b}} = \begin{Bmatrix} \boldsymbol{0} \\ \boldsymbol{b} \end{Bmatrix}$$

and where $\boldsymbol{G}$ is any nonsingular matrix but is usually taken to be $\boldsymbol{A}_0$. The homogeneous solutions for $i = 1, 2, \ldots, 2m$ of Eq. (29) are solutions of the eigenvalue problem

$$\mathcal{A}\boldsymbol{x}_i = \lambda_i \mathcal{B}\boldsymbol{x}_i \tag{30}$$

By convention, we order the eigenvalues from smallest to largest in magnitude. Equation (30) may be expressed more compactly by

$$\mathcal{A}\boldsymbol{X} = \mathcal{B}\boldsymbol{X}\boldsymbol{\Lambda} \tag{31}$$

where $\boldsymbol{X}$ is a matrix whose $i$th column is the eigenvector $\boldsymbol{x}_i$ and $\boldsymbol{\Lambda}$ is a diagonal matrix whose $i$th entry is the corresponding eigenvalue $\lambda_i$. Similarly, the left eigenvalue problem is defined by

$$\mathcal{A}^T\boldsymbol{Y} = \mathcal{B}^T\boldsymbol{Y}\boldsymbol{\Lambda} \tag{32}$$

Finally, it can be shown that the left and right eigenvectors, if suitably normalized, satisfy the biorthogonality conditions

$$\boldsymbol{Y}^T\mathcal{B}\boldsymbol{X} = \boldsymbol{I}, \qquad \boldsymbol{Y}^T\mathcal{A}\boldsymbol{X} = \boldsymbol{\Lambda} \tag{33}$$

Next, to find the particular solutions to Eq. (29), we use the right eigenvectors as basis functions, i.e., we let

$$\boldsymbol{U} = \boldsymbol{X}\boldsymbol{w} \tag{34}$$

where $\boldsymbol{w}$ is a vector whose $i$th entry describes how much of the $i$th eigenmode is present in the solution. Therefore, Eq. (29) becomes

$$\mathcal{A}\boldsymbol{X}\boldsymbol{w} - j\omega\mathcal{B}\boldsymbol{X}\boldsymbol{w} = \bar{\boldsymbol{b}} \tag{35}$$

Next, we premultiply Eq. (35) by the left eigenvectors $\boldsymbol{Y}$. Making use of the biorthogonality properties of the left and right eigenvectors, the result is a set of $2m$ uncoupled scalar equations of the form

$$\lambda_i w_i - j\omega w_i = \kappa_i, \qquad i = 1, 2, \ldots, 2m \tag{36}$$

where $\kappa_i$ is the so-called participation factor given by $\boldsymbol{y}_i^T\bar{\boldsymbol{b}}$. Finally, solving for all of the $w_i$ and combining with Eq. (34) gives the desired solution

$$\boldsymbol{U} = \sum_{i=1}^{2m} w_i\boldsymbol{x}_i = \sum_{i=1}^{2n} \frac{\kappa_i}{\lambda_i - j\omega}\boldsymbol{x}_i \tag{37}$$

In principle, Eq. (37) is exact because all of the eigenmodes have been used and, except in degenerate cases, the eigenvectors form a complete basis. In practice, however, one would truncate the series retaining only the dominant low-frequency eigenmodes. Thus, the sum is truncated at $i = k$, where $k \ll 2m$. Using this approach, however, one finds that the computed solution may differ significantly from the exact solution, even though $|\lambda_k| \gg \omega$. Therefore, to improve the estimate of the solution, we use the method of multiple static corrections. A simple algebraic manipulation of Eq. (37) gives

$$\boldsymbol{U} = \sum_{i=1}^{2m} \left(\frac{j\omega}{\lambda_i}\right)^{M_c} \frac{\kappa_i}{\lambda_i - j\omega}\boldsymbol{x}_i + \sum_{r=1}^{M_c} (j\omega)^{r-1}\boldsymbol{U}^r_{\text{static}} \tag{38}$$

where $M_c$ is the number of static corrections and

$$\mathcal{A}\boldsymbol{U}^1_{\text{static}} = \bar{\boldsymbol{b}}$$

and for $r > 1$

$$\mathcal{A}\boldsymbol{U}^{r}_{\text{static}} = \mathcal{B}\boldsymbol{U}^{r-1}_{\text{static}}$$

For a derivation of the method of multiple static corrections, see Ref. 34.

Note that the first series in Eq. (38) is identical to the series in Eq. (37) with each term multiplied by $(j\omega/\lambda_i)^{M_c}$. Thus, the first series in Eq. (38) will converge more quickly than the series in Eq. (37). Furthermore, the static correction terms $\boldsymbol{U}^{r}_{\text{static}}$ can be efficiently and repeatedly computed if the matrix $\mathcal{A}$ has been decomposed into LU factors.

Finally, construction of reduced-order models as just described requires that a large, sparse, complex, nonsymmetric, generalized eigenvalue problem be solved. The authors have implemented a generalized nonsymmetric Lanczos algorithm with full reorthogonalization.[34] For both the eigensolver and the reduced-order model, the quadratic nature of the equations is taken into account, improving the efficiency of the algorithms. For example, the problems considered in this paper solved on the medium grid have around 26,000 degrees of freedom. Using one processor of a Silicon Graphics Origin 2000 computer, a single conventional unsteady flow calculation (a single interblade phase angle and frequency) requires about 160 CPU s. By way of comparison, approximately 360 s of computer time was required to generate a single reduced-order model (a single interblade phase angle). However, once computed, the unsteady aerodynamic response can be computed in less than 1 s for each desired reduced frequency.

### B. Computational Results

*1. Eigenvalues and Eigenmodes of the Unsteady Flow*

Shown in Fig. 5 are the eigenvalues of the unsteady flow for the cascade described in Sec. III.C for the case where the steady inflow angle is 55 deg. Shown are the eigenvalues of fluid motion for seven different interblade phase angles. All of the eigenvalues are in the left half plane, indicating that the system is fluid dynamically stable. (This does not preclude the possibility that the system is aeroelastically unstable as in Fig. 4a.) For low-frequency excitations, e.g., $\bar{\omega} \leq 1$, the dynamic response of the fluid will be dominated by the two eigenvalue clusters located just to the left of the origin near the real axis. The least stable of the eigenvalues in this group corresponds to smaller interblade phase angles. Also note the generally vertical line of eigenvalues to the left. These eigenvalues are thought to form a discrete representation of a branch cut in the aerodynamic transfer function.[15]

The behavior of the eigenvalues as the inflow angle is increased is of some interest because at large incidences the flow may become fluid dynamically unstable. In particular, one would expect to see evidence of a linear instability related to rotating stall as the inflow angle is increased. Shown in Fig. 6 are the eigenvalue loci for an inflow angle $\Omega$ of 61.5 deg. Note the dramatic change in the form of the two primary loci located near the origin. The two loci are now located very near the origin, one above the real axis and one below.

Of particular interest are the low interblade phase angle eigenvalues appearing in the cluster nearest the origin. Consider, for example, the two $\sigma = -45$ deg eigenvalues. One has a positive frequency (positive imaginary part) and a slow decay rate (small negative real part). The positive frequency in combination with a negative interblade phase angle implies a wave moving in the rotor frame opposite the direction of rotation. The phase speed $V_p$ is equal to $-\text{Im}(\lambda)G/\sigma$, where $G$ is the blade-to-blade gap. For this example, the phase speed is approximately 0.194 times the relative inflow velocity $V$. Similarly, the phase speed of the lightly damped $\sigma = -90$ deg mode is $0.144 \times V$. Although the modes are not unstable, these lightly damped modes are likely the modes that will initiate rotating stall at higher incidence angles. To illustrate this point, Fig. 7 shows an expanded view of the eigenvalues near the origin for different interblade phase angles as the inflow angles $\Omega$ varies from 55 to 61.5 deg. Note that the least stable eigenvalue moves to the right as the incidence is increased. Extrapolating, it appears that this mode will become neutrally stable at an inflow angle of around

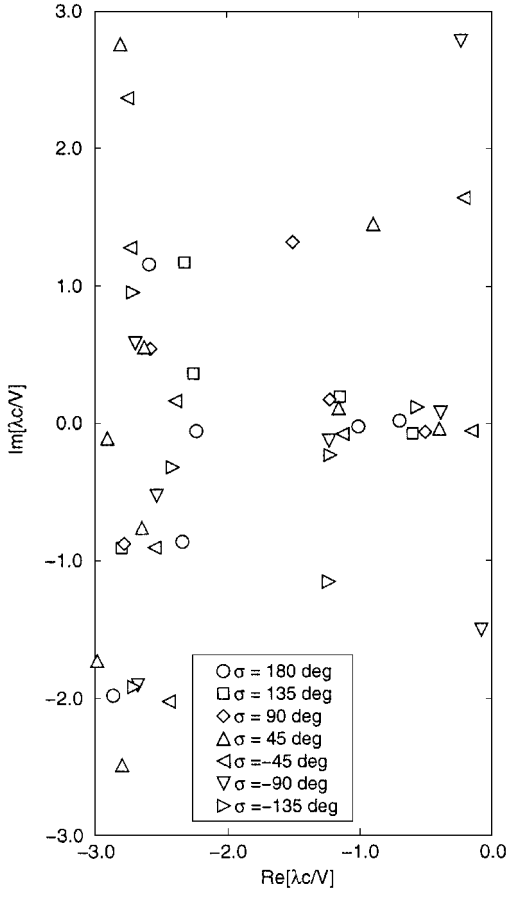


**Fig. 5 Eigenvalues of low-speed unsteady flow about cascade for various interblade phase angles, $\Omega$ = 55 deg.**

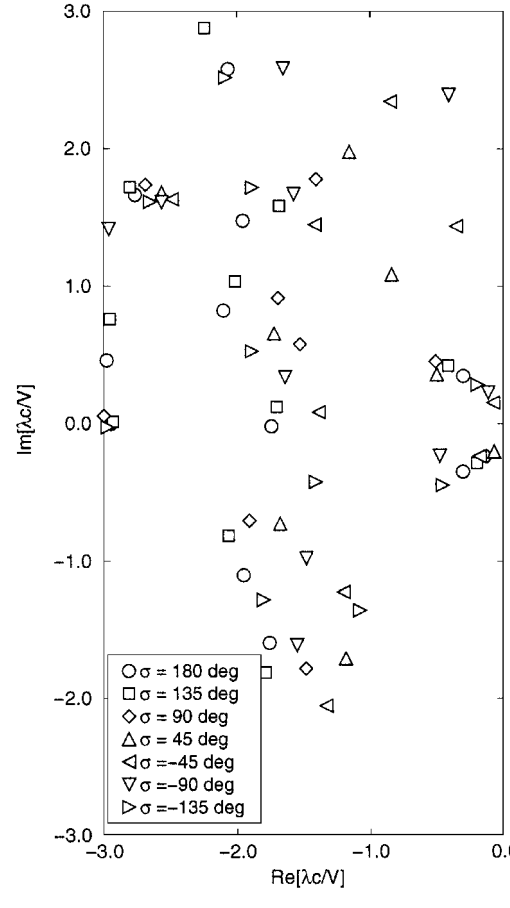


**Fig. 6 Eigenvalues of low-speed unsteady flow about cascade for various interblade phase angles, $\Omega$ = 61.5 deg.**

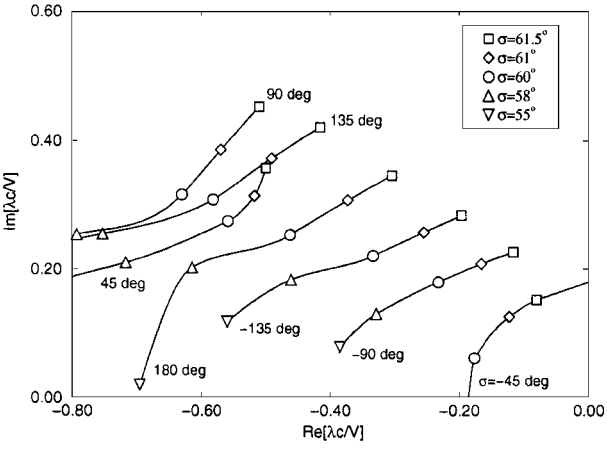


**Fig. 7 Eigenvalues of low-speed unsteady flow about cascade for various inflow angles and interblade phase angles.**

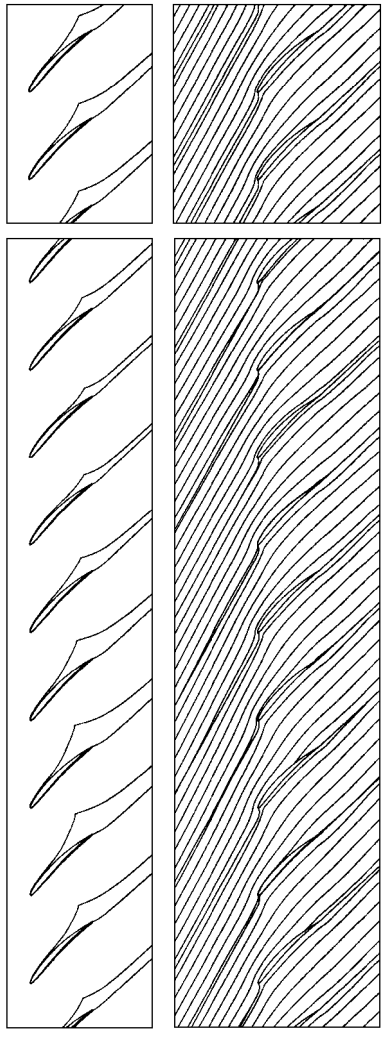

**Fig. 8 Top, left to right, steady flow quantities: displacement thickness $\Delta^*$ (exaggerated for clarity) and inviscid streamfunction $\Psi_{inv}$ for cascade operating at $\Omega = 61.5$ deg. Bottom, left to right, unsteady flow quantities: displacement thickness $\Delta^* + \delta^* e^{\lambda t}$ (exaggerated) and inviscid streamfunction $\Psi_{inv} + \psi_{inv} e^{\lambda t}$ (exaggerated).**

62.3 deg resulting in a phase speed of $0.229 \times V$ for the neutrally stable eigenmode. Unfortunately, we were unable to test this hypothesis because the steady flow solver did not converge at high inflow angles. Figure 8 shows the computed unsteady eigenmode corresponding to this eigenvalue for an inflow angle $\Omega$ of 61.5 deg. This eigenmode is qualitatively similar to the model of rotating stall proposed by Emmons et al.,[41] with a stall cell rotating circumferentially through the cascade in the direction opposite to the direction

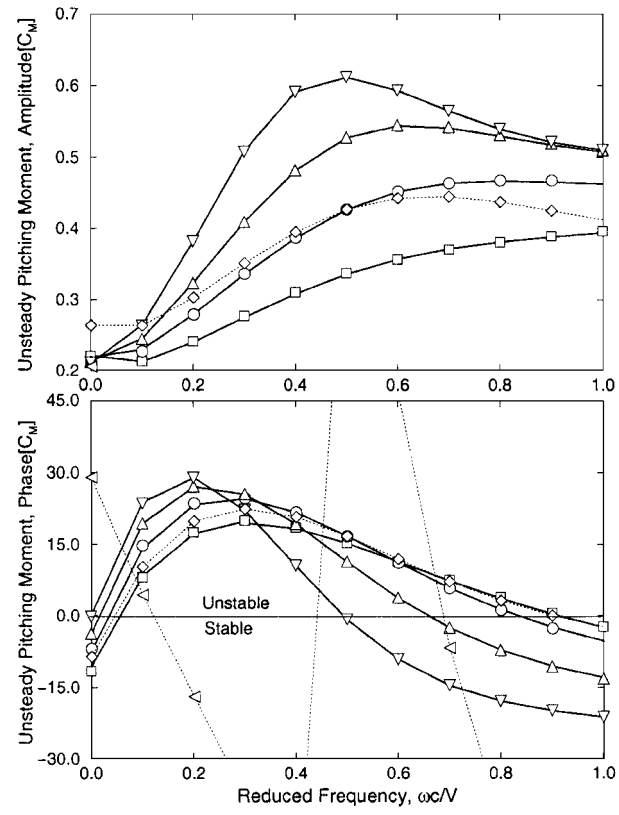


**Fig. 9 Amplitude and phase of pitching moment for airfoils pitching about a point near midchord for a range of reduced frequencies, $\Omega = 61.5$ deg: reduced-order model with three static corrections at □, $\sigma = 45$ deg; ○, $\sigma = 90$ deg; Δ, $\sigma = 135$ deg; and ▽, $\sigma = 180$ deg; ——, exact solution; reduced-order model for $\sigma = 90$ deg case with ◁, zero, and ◇, one static correction.**

of rotation (in the rotor frame of reference) at a fraction of the relative inflow velocity. Note that the streamlines are slightly diverted around the the passages with the largest flow separations. This causes the incidence to increase on the airfoils above the blockage and to decrease on the airfoils below the blockage. This in turn causes the separation to grow on the airfoils above and diminish on the airfoils below. Thus, the pattern tends to propagate upward through the cascade.

*2. Reduced-Order Models of the Unsteady Flow*

Next we construct a reduced-order model of the unsteady flowfield using the eigeninformation found in the preceding section. In particular, we consider the case where the inflow angle $\Omega$ is 61.5 deg, and the interblade phase angle $\sigma$ varies from 45 to 180 deg. For each interblade phase angle considered, a new reduced-order model must be constructed. For the cases presented here, a frequency shift $\omega_0 = 0.5$ is used, and all of the eigenmodes with reduced eigenvalues $(\lambda c/V)$ within a radius of 1.5 of $j\omega_0$ are considered. Shown in Fig. 9 are the computed amplitude and phase angle of the pitching moment for the cascade, where the airfoils pitch with different interblade phase angles and for a range of reduced frequencies. Shown for comparison are the pitching moment computed using the direct solver and the pitching moment computed using the reduced-order model with zero, one, and three static corrections. Note that with no static corrections, the reduced-order model does a very poor job of predicting the moment, even at very low reduced frequencies. With one static correction, the reduced-order model results have a similar trend as the exact solution, but are qualitatively different, especially away from the shift frequency $\omega_0$. With three static corrections, the agreement is very good over the entire frequency range.

Some physical insight into why the aerodynamic damping behaves as it does (Fig. 9) can be gleaned by examination of Fig. 7. Note that for $\Omega = 61.5$ deg, the damping ratio of the eigenvalues decreases as the interblade phase angle $\sigma$ goes from 45 to 180 deg. Hence, the corresponding eigenmodes, which are expected

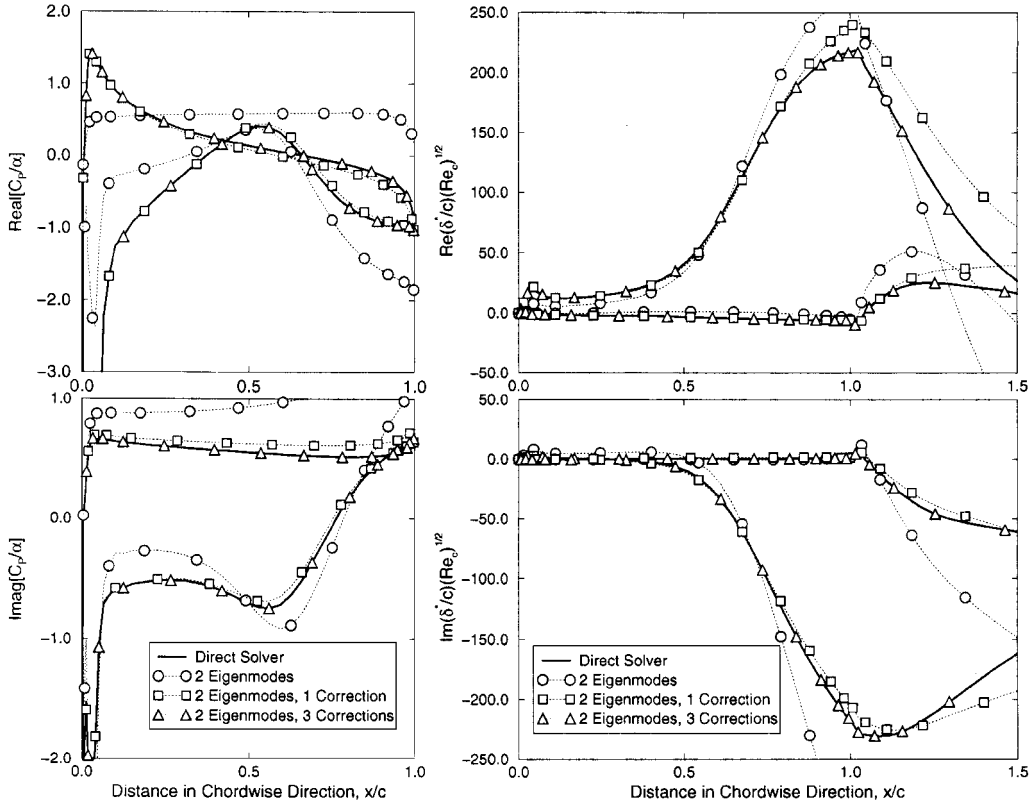


**Real and imaginary parts of unsteady coefficient of pressure** **Unsteady displacement thickness**

**Fig. 10 Airfoils pitching about a point near midchord, $\Omega$ = 61.5 deg, $\sigma$ = 90 deg, and $\bar{\omega}$ = 0.3.**

to contribute significantly to the aerodynamic response because of the proximity of the eigenvalues to the prescribed vibratory frequency [Eq. (38)], should have stronger resonant responses as the interblade phase angle is increased. This is clearly seen to be the case in Fig. 9. For example, the $\sigma = 180$ deg case, which corresponds to the most lightly damped eigenvalue, also has a noticeable peak in the amplitude of the aerodynamic response.

Conversely, for a fixed interblade phase angle $\sigma$ of 90 deg, the damping of the (low-frequency) eigenmode decreases substantially with increasing inflow angle $\Omega$. Thus, the contribution of this mode is expected to increase substantially, especially for vibratory frequencies near the mode resonance. This may explain the dramatic change in the aerodynamic response seen in Fig. 4a for a reduced frequency $\bar{\omega}$ of 0.5 as the inflow angle is increased. For a reduced frequency $\bar{\omega}$ of 1.0, on the other hand, there are no eigenvalues near the forcing frequency. Hence, the aerodynamic response will be less sensitive to the movement of the eigenvalues, as is seen to be the case in Fig. 4b.

Figure 10 shows the real and imaginary parts of the unsteady coefficient of pressure and the unsteady displacement thickness computed using the direct method and the reduced-order model for pitching motion with a reduced frequency $\bar{\omega}$ of 0.3. Again, the solution computed with the reduced-order model is in good agreement with the direct solution, provided that three static corrections are used. The implication is that both gross flow features, e.g., the unsteady pitching moment, and details of the unsteady flowfield, e.g., the displacement, can be accurately predicted with reduced-order models, although the detailed flow features may require more static corrections.

## V. Summary and Conclusions

A linearized viscous–inviscid interaction model of unsteady flows in cascades is presented. The outer inviscid flow is modeled by the full potential equation, which is discretized using a variational finite element method. The inner inviscid flow is modeled by the boundary-layer equations, with a one-equation turbulence model. The inner flow equations are discretized using finite differences. An injection boundary condition is used to simultaneously couple the inner and outer regions.

Two approaches are used to solve the discretized unsteady small-disturbance equations, which describe the unsteady viscous flow in a cascade. Using the conventional approach, a large sparse matrix equation is formed for each steady flow condition, reduced frequency, and interblade phase angle of interest, and then is solved using LU decomposition. Alternatively, for each steady flow condition and interblade phase angle, one can compute the eigenfrequencies and corresponding eigenmodes of fluid motion by solving a large, sparse, complex, quadratic eigenvalue problem. Then, using the resulting eigeninformation, one can construct low-order reduced-order models of the unsteady flow.

A number of numerical examples were presented. For example, the aerodynamic damping for torsional vibrations of the Tenth Standard Configuration was examined using the conventional linearized unsteady flow solver at four inflow angles and two reduced frequencies for a range of interblade phase angles. Furthermore, for the highest incidence case considered ($\Omega = 61.5$ deg), the aerodynamic damping was computed for an interblade phase angle $\sigma$ of 90 deg for a range of reduced frequencies. Generally, it was found that the system was less stable at lower reduced frequencies and higher incidences. These results are consistent with empirical trends for torsional stall flutter.

Reduced-order aerodynamic models of the unsteady flowfield were constructed. Importantly, the reduced-order aerodynamic models are low-degree-of-freedom models that are computationally very efficient. The major computational cost is in the computation of the dominant eigenvalues and corresponding eigenmodes. Once these have been computed, however, the computational cost of computing the aerodynamic response is minimal. It was found that very accurate aerodynamic models can be constructed using just two eigenmodes, provided that the static correction technique is applied. The physical implication is that the unsteady aerodynamic response may be thought of as composed of two parts: a quasisteady part plus a dynamic perturbation. The dynamic perturbation is dominated by the response of just a handful of eigenmodes.

Finally, the eigenvalues and eigenmodes of the linearized unsteady flow model provide important physical insight into the physics of the unsteady flow about the cascade of airfoils and may prove useful for predicting the onset of fluid dynamic instabilities such as rotating stall.

## Acknowledgments

This work was supported in part by the National Science Foundation under Grant CTS-9157908. The U. S. government has certain rights in this material. We are grateful to William S. Clark, a Ph.D. student at Duke University currently employed at Allison Engine Company, for the Navier–Stokes analysis results used for the comparison shown in Fig. 2.

## References

[1]Sisto, F., "Stall Flutter," *AGARD Manual on Aeroelasticity in Axial Flow Turbomachines, Unsteady Turbomachinery Aerodynamics*, edited by M. F. Platzer and F. O. Carta, AGARD-AG-298, Vol. 1, Neuilly sur Seine, France, 1987, Chap. 7.

[2]Greitzer, E. M., "Surge and Rotating Stall in Axial Flow Compressors. Part I: Theoretical Compression System Model," *Journal of Engineering for Power*, Vol. 98, April 1976, pp. 190–198.

[3]Moore, F. K., and Greitzer, E. M., "A Theory of Post-Stall Transients in Axial Compression Systems: Parts I and II," *Journal of Engineering for Gas Turbines and Power*, Vol. 108, No. 1, 1986, pp. 68–76.

[4]Whitehead, D. S., "The Vibration of Cascade Blades Treated by Actuator Disc Methods," *Proceedings of the Institution of Mechanical Engineering*, Vol. 173, No. 21, 1959, pp. 555–563.

[5]Whitehead, D. S., "Bending Flutter of Unstalled Blades at Finite Deflection," Aeronautical Research Council, Repts. and Memoranda 3386, London, Oct. 1962.

[6]Kaji, S., and Okazaki, T., "Cascade Flutter in Compressible Flow," *Transactions of the Japan Society of Mechanical Engineers*, Vol. 38, No. 309, pp. 1023–1033.

[7]Adamczyk, J. J., Stevens, W., and Jutras, R., "Supersonic Stall Flutter of High Speed Fans," *Journal of Engineering for Power*, Vol. 104, No. 3, 1982, pp. 675–682.

[8]Gysling, D. L., and Myers, M. R., "A Framework for Analyzing the Dynamics of Flexibly-Bladed Turbomachines," 41st American Society of Mechanical Engineers (ASME) International Gas Turbine and Aeroengine Congress and Exposition, ASME Paper 96-GT-440, Birmingham, UK, June 1996.

[9]Dowell, E. H., "A Simple Method for Converting Frequency Domain Aerodynamics to the Time Domain," NASA TM-81844, Oct. 1980.

[10]Peterson, L. D., and Crawley, E. F., "Improved Exponential Time Series Approximation of Unsteady Aerodynamic Operators," *Journal of Aircraft*, Vol. 25, No. 2, 1988, pp. 121–127.

[11]Eversman, W., and Tewari, A., "Consistent Rational-Function Approximation for Unsteady Aerodynamics," *Journal of Aircraft*, Vol. 28, No. 9, 1991, pp. 545–552.

[12]Eversman, W., and Tewari, A., "Modified Exponential Series Approximation for the Theodorsen Function," *Journal of Aircraft*, Vol. 28, No. 9, 1991, pp. 553–557.

[13]Dunn, H. J., "An Analytical Technique for Approximating Unsteady Aerodynamics in the Time Domain," NASA TP-1738, Nov. 1980.

[14]Mahajan, A. J., Dowell, E. H., and Bliss, D. B., "Eigenvalue Calculation Procedure for Euler/Navier–Stokes Solvers with Application to Flows over Airfoils," *Journal of Computational Physics*, Vol. 97, No. 2, 1991, pp. 398–413.

[15]Hall, K. C., "Eigenanalysis of Unsteady Flows About Airfoils, Cascades, and Wings," *AIAA Journal*, Vol. 32, No. 12, 1994, pp. 2426–2432.

[16]Hall, K. C., Florea, R., and Lanzkron, P. J., "A Reduced Order Model of Unsteady Flows in Turbomachinery," *Journal of Turbomachinery*, Vol. 117, No. 3, 1995, pp. 375–383.

[17]Florea, R., and Hall, K. C., "Reduced Order Modeling of Unsteady Flows About Airfoils," *Aeroelasticity and Fluid Structure Interaction Problems*, AD-Vol. 44, edited by P. P. Friedman and J. C. I. Chang, American Society of Mechanical Engineers, New York, 1994, pp. 49–68.

[18]Romanowski, M. C., and Dowell, E. H., "Using Eigenmodes to Form an Efficient Euler Based Unsteady Aerodynamics Analysis," *Aeroelasticity and Fluid Structure Interaction Problems*, AD-Vol. 44, edited by P. P. Friedman and J. C. I. Chang, American Society of Mechanical Engineers, New York, 1994, pp. 147–160.

[19]Romanowski, M. C., and Dowell, E. H., "Aeroelastic Analysis of an Airfoil Using Eigenmode Based Reduced Order Unsteady Aerodynamics," *Proceedings of the AIAA/ASME/ASCE/AHS/ASC 36th Structures, Structural Dynamics, and Materials Conference and AIAA/ASME Adaptive Structures Forum* (New Orleans, LA), Pt. 3, AIAA, Washington, DC, 1995, pp. 1863–1870 (AIAA Paper 95-1380).

[20]Cizmas, P. G., and Hall, K. C., "Computation of Steady and Unsteady Viscous Flows Using a Simultaneously Coupled Inviscid-Viscous Interaction Technique," *Journal of Fluids and Structures*, Vol. 9, No. 6, 1995, pp. 639–657.

[21]Cizmas, P. G. A., and Hall, K. C., "A Viscous-Inviscid Model of Unsteady Small Disturbance Flows in Cascades," AIAA Paper 95-2655, July 1995.

[22]Spalart, P. R., and Allmaras, S. R., "A One-Equation Turbulence Model for Aerodynamics Flows," *La Recherche Aérospatiale*, No. 1994-1, 1994, pp. 5–21.

[23]Cebeci, T., and Bradshaw, P., *Momentum Transfer in Boundary Layers*, Hemisphere, Washington, DC, 1977, pp. 97–101, 235–280.

[24]Catherall, D., and Mangler, K. W., "The Integration of the Two-Dimensional Laminar Boundary-Layer Equations Past the Point of Vanishing Skin Friction," *Journal of Fluid Mechanics*, Vol. 26, Pt. 2, 1966, pp. 63–182.

[25]Le Balleur, J. C., "Couplage Visqueux-Non Visqueux: Methode Numerique et Applications aux Écoulement Bidimensionnels Transoniques et Supersoniques," *La Recherche Aérospatiale*, No. 1978-2, 1978, pp. 65–76.

[26]Kwon, O. K., and Pletcher, R. H., "Prediction of Incompressible Separated Boundary Layers Including Viscous-Inviscid Interaction," *Journal of Fluids Engineering*, Vol. 101, No. 4, 1979, pp. 466–472.

[27]Carter, J. E., "A New Boundary-Layer Inviscid Iteration Technique for Separated Flow," AIAA Paper 79-1450, 1979.

[28]Barnett, M., Hobbs, D. E., and Edwards, D. E., "Inviscid-Viscous Interaction Analysis of Compressor Cascade Performance," *Journal of Turbomachinery*, Vol. 113, No. 4, 1991, pp. 538–552.

[29]Barnett, M., Verdon, J. M., and Ayer, T. C., "Analysis of High Reynolds Number Inviscid–Viscid Interaction in Cascades," *AIAA Journal*, Vol. 31, No. 11, 1993, pp. 1969–1976.

[30]Veldman, A. E. P., "New, Quasi-simultaneous Method to Calculate Interacting Boundary Layers," *AIAA Journal*, Vol. 19, No. 1, 1981, pp. 79–85.

[31]Brune, G. W., Rubbert, P. E., and Nark, T. C., "New Approach to Inviscid Flow/Boundary Layer Matching," *AIAA Journal*, Vol. 13, No. 7, 1975, pp. 936–938.

[32]Moses, H. L., Jones, R. R., and O'Brien, W. F., "Simultaneous Solution of the Boundary Layer and Freestream with Separated Flow," *AIAA Journal*, Vol. 16, No. 1, 1978, pp. 61–66.

[33]Drela, M. B., Giles, M., and Thompkins, W. T., "Newton Solution of Coupled Euler and Boundary Layer Equations," *The Third Symposium on Numerical and Physical Aspects of Aerodynamic Flows (Long Beach, CA)*, edited by T. Cebeci, Springer–Verlag, Berlin, 1985, pp. 143–154.

[34]Florea, R., "Reduced Order Modelling and Eigenvalue Analysis of Unsteady Flows About Oscillating Airfoils and Turbomachinery Cascades," Ph.D. Thesis, Dept. of Mechanical Engineering and Materials Science, Duke Univ., Durham, NC, Dec. 1996.

[35]Hall, K. C., Lorence, C. B., and Clark, W. S., "Nonreflecting Boundary Conditions for Linearized Unsteady Aerodynamic Calculations," AIAA Paper 93-0882, Jan. 1993.

[36]Hall, K. C., "Deforming Grid Variational Principle for Unsteady Small Disturbance Flows in Cascades," *AIAA Journal*, Vol. 31, No. 5, 1993, pp. 891–900.

[37]Bateman, H., "Irrotational Motion of a Compressible Fluid," *Proceedings of the National Academy of Sciences of the United States*, Vol. 16, 1930, pp. 816–825.

[38]Keller, H. B., and Cebeci, T., "Accurate Numerical Methods for Boundary Layer Flows. Two Dimensional Laminar Flows," *Proceedings of the Second International Conference on Numerical Methods in Fluid Dynamics*, Vol. 8, Lecture Notes in Physics, Springer–Verlag, Berlin, 1971, pp. 92–100.

[39]Fransson, T. H., and Verdon, J. M., "Panel Discussion on Standard Configurations for Unsteady Flow Through Vibrating Axial-Flow Turbomachine Cascades," *Unsteady Aerodynamics, Aeroacoustics, and Aeroelasticity of Turbomachines and Propellers*, edited by H. M. Atassi, Springer–Verlag, New York, 1993, pp. 859–889.

[40]Clark, W. S., and Hall, K. C., "A Numerical Model of the Onset of Stall Flutter in Cascades," 40th American Society of Mechanical Engineers (ASME) International Gas Turbine and Aeroengine Congress and Exposition, ASME Paper 95-GT-377, Houston, TX, June 1995.

[41]Emmons, H. W., Pearson, C. E., and Grant, H. P., "Compressor Surge and Stall Propagation," *Transactions of the American Society of Mechanical Engineers*, Vol. 77, May 1955, pp. 450–469.

S. Fleeter
*Associate Editor*